Navier-Stokes-Based Dynamic Simulations of Sling Loads

Daniel T. Prosser* and Marilyn J. Smith†

School of Aerospace Engineering, Georgia Institute of Technology, Atlanta, GA, USA

Computational fluid dynamics (CFD) is used to resolve the unsteady Navier Stokes equations for prediction of aerodynamic forces and moments acting on dynamic helicopter sling loads. The six-degree-of-freedom (6-DOF) rigid-body equations are tightly coupled with CFD to simulate body motion, and a model of the cables is developed to provide constraint forces and moments. This work presents the methodology and results of the coupled simulations with validation against experimental data. In addition, integration schemes for the 6-DOF equations are evaluated, and the effect of feature-based grid adaptation is investigated. Results of the simulations demonstrate good correlation with available experimental data and also show that the cable model assumptions are important in the dynamic behavior of the sling load.

Nomenclature

u, v, w	Velocity components in the body frame
p, q, r	Angular velocity components in the body frame
V_x, V_y, V_z	Velocity components in the inertial frame
$\vec{e}_r$	Radial-direction unit vector
$\vec{F}$, $\vec{M}$	Force and moment vectors
T	Cable tension
F_s, F_d	Spring and damper forces
F_c, M_c	Total constraint force and moment applied by cables
P, O	Cable attachment points on body and fixed space
I	Inertia tensor
e_0, e_1, e_2, e_3	Quaternions
s	Numerical order of accuracy
β	Yaw angle
ω_n	Natural frequency, $\omega_n = \sqrt{k/m}$
σ	Damping ratio
Δt	Time step
Re	Reynolds number, $Re = \rho V_{ref} L_{ref}/\mu$
Subscript	
n	Time level
r	Radial component
i	Cable number

I. Introduction

A major benefit of helicopters and other rotor-based vertical lift vehicles is their versatility in being able to transport diverse loads to remote or precarious locations. Loads attached by cables underneath the rotorcraft are referred to as *sling loads*. This method of transporting loads is very common in both military and civilian operations because of the wide range of load types that can be attached in this way.

*Graduate Research Assistant, AIAA student member.

†Associate Professor, AIAA Associate Fellow.

However, in practice a number of difficulties arise in sling load operations. In general, sling loads are not designed for aerodynamic efficiency and as such usually can be classified aerodynamically as bluff bodies. In forward flight, the unsteady wake shed from the sling load results in periodic oscillations of the load. The magnitude of oscillation increases with flight speed as the unsteady aerodynamic forces become stronger, resulting in a dangerous condition in which the sling load may be lost, the rotorcraft and crew may be put in danger, or both. Therefore, it is important that for any sling load configuration, a safe flight envelope must be determined prior to operation.

Currently, flight envelope validation for sling loads is carried out via flight testing, which is expensive and time-consuming.[1] Substantial savings are possible by migrating to flight envelope validation based on computational simulation and wind tunnel testing. However, bluff bodies are challenging for aerodynamic analysis in that they produce large unsteady, turbulent wakes with periodic separation and reattachment,[2] precluding the use simplistic aerodynamic models that neglect these phenomena. In addition, in some flight conditions the rotor wake may impinge on the load, further complicating both numerical and experimental aerodynamics predictions.

In addition to aerodynamic complexities, the system dynamics must also be considered. Variations in cable attachment geometry and materials may have a significant effect on dynamic response of the sling load,[3] and widely varying sling geometries and systems used in operations introduce challenges in developing a generalized model for use in simulation. Furthermore, the rotorcraft and sling load make up a coupled system in which the rotorcraft's dynamics can affect the sling load, and vice-versa. Due to complexity and size constraints, in most cases it is not possible to investigate the coupled system dynamics in a wind tunnel, and in computational analyses the added complexity results in significantly higher cost.

There have been a number of recent efforts to understand sling load dynamics and aerodynamics. Raz et al.[4] and Cicolani et al.[5] used wind tunnel testing while focusing on passive stabilization of sling load dynamics. They reported good correlation of wind tunnel results with flight testing and demonstrated that higher safe flight speeds could be reached in sling loads operations by the addition of aerodynamic fins. Raz et al.[1] used wind tunnel testing and flight test data to investigate several important aspects of sling loads operations, including coupled helicopter-load dynamics, pilot induced oscillations, and most notably that carefully-implemented wind tunnel testing of scaled sling load models can give good correlation with flight test data. Others have approached the problem using simulation instead of wind tunnel testing. For example, Cicolani and da Silva[6] used computational fluid dynamics (CFD) and dynamic simulation in a one-way coupling approach. In that study, unsteady aerodynamic characteristics of the load were first simulated using two-dimensional CFD and used to construct a forcing function for the sling load dynamics in frequency-domain response analysis. A similar approach was also used by Cicolani et al.,[7] but with the aerodynamic model augmented by wind tunnel and three-dimensional CFD data.

Theron et al.[8] simulated the aerodynamics of a spinning load in prescribed motion about a fixed axis using three-dimensional CFD and a variety of turbulence models to demonstrate that CFD is capable of predicting aerodynamic force coefficients accurately when the load is in motion. Further testing of various CFD codes, turbulence models, and load geometries was carried out by Theron et al.[9] in both steady and prescribed dynamic motion. Mantri et al.[10] used wind tunnel testing as well as two-dimensional and three-dimensional CFD to investigate the aerodynamics and dynamics of sling loads. One key result of the CFD studies performed therein is that two-dimensional CFD may be appropriate only for a small range of flow regimes seen in sling loads operations, but to capture all of the aerodynamic phenomena during sling loads simulation a fully three-dimensional grid and turbulence model are required. Greenwell[2] and Prosser and Smith[11] have demonstrated that the requirement for three-dimensional aerodynamic analysis are a result of complex flow features such as separation, reattachment, and relief effects which become dominant at different orientation angles relative the flow direction.

The goal of the present research is to improve the understanding of the complex physics of dynamic bluff bodies (in particular, sling loads) using high-fidelity unsteady Navier-Stokes-based computational aerodynamics coupled with computational dynamics in a two-way coupling fashion. In previous sling loads studies involving CFD simulation, CFD was used to extract static aerodynamic data or limited dynamic data for later use in simulation models or comparison with wind tunnel and flight test data[6–10] . In the present paper, the dynamics and aerodynamics of a sling load configuration are simulated simultaneously using CFD coupled with a library to compute the dynamic response of the load. The ultimate goal of this research is to investigate whether modern computational approaches are sufficient to predict the physical behavior of this complex system so that in the future less flight testing will be required for operational validation

of sling-load missions. In this work, the methodology used for Navier-Stokes-based dynamic simulations is presented, along with results of simulations and correlation with experimental data.

II. FUN3D Code

High-fidelity sling loads analysis requires a computational tool able to capture highly separated and unsteady turbulent wakes over a broad range of Reynolds numbers and Mach numbers. Sling load dynamics involve large oscillations, which means that overset grid capability is required for dynamic simulations. The CFD code FUN3D, developed at NASA Langley, is used in this research to fulfill these requirements. FUN3D solves the Navier-Stokes equations using an implicit finite-volume approach on unstructured mixed element grids.[12,13] Grid adaptation is leveraged to improve the capture of the turbulent wake region.[14] A number of turbulence modes are available, including Spalart-Allmaras, Menter kω-SST, Detached-Eddy Simulation, and hybrid RANS-LES. In this work, the hybrid RANS-LES model is chosen because it is appropriate for unsteady flows with large separated regions.[15,16]

The dynamic simulation of sling loads also requires the CFD code to be able to handle moving bodies with large degrees of displacement and rotation. In FUN3D, the overset grid option is employed to allow for these types of simulations. Overset grid mechanics and interpolation are controlled through the DiRTLib[17] (Donor Receptor Transaction Library) and SUGGAR++[18] (Structured, Unstructured, and Generalized Grid AssembleR) libraries.

III. Six-Degree-of-Freedom Simulation

The six-degree-of-freedom (6-DOF) motion of a rigid body may be described completely using a system of first-order ordinary differential equations. The equations are written in the moving body frame so that the rotational inertia tensor is constant. The four-parameter quaternion formulation may be used to describe the orientation of the rigid moving body without any singularities.[19] This formulation leads to the following system of thirteen equations to be solved simultaneously

$$
\begin{aligned}
&\dot{u} = \frac{1}{m}\left(F_x + vr - wq\right) \quad \dot{v} = \frac{1}{m}\left(F_y - ur + wp\right) \quad \dot{w} = \frac{1}{m}\left(F_z + uq - vp\right) \\
&\dot{p}I_{xx} - \dot{q}I_{xy} - \dot{r}I_{xz} = M_x + qr\left(I_{yy} - I_{zz}\right) + \left(q^2 - r^2\right)I_{yz} - prI_{xy} + pqI_{xz} \\
&-\dot{p}I_{xy} + \dot{q}I_{yy} - \dot{r}I_{yz} = M_y + pr\left(I_{zz} - I_{xx}\right) + \left(r^2 - p^2\right)I_{xz} - pqI_{yz} + qrI_{xy} \\
&-\dot{p}I_{xz} - \dot{q}I_{yz} + \dot{r}I_{zz} = M_z + pq\left(I_{xx} - I_{yy}\right) + \left(p^2 - q^2\right)I_{xy} - qrI_{xz} + prI_{yz} \\
&\dot{e_0} = \frac{1}{2}\left(-e_1 p - e_2 q - e_3 r\right) \\
&\dot{e_1} = \frac{1}{2}\left(e_0 p - e_3 q + e_2 r\right) \\
&\dot{e_2} = \frac{1}{2}\left(e_3 p + e_0 q - e_1 r\right) \\
&\dot{e_3} = \frac{1}{2}\left(-e_2 p + e_1 q + e_0 r\right) \\
&\dot{X} = V_x \quad \dot{Y} = V_y \quad \dot{Z} = V_z
\end{aligned}
\tag{1}
$$

where the force and moment components are given in the moving body frame. There are two contributions to these forces and moments: aerodynamics computed by FUN3D and constraint forces and moment computed by the cable model. The positions X, Y, and Z as well as the velocities V_x, V_y, and V_z are given in the inertial frame. V_x, V_y, and V_z are calculated from the moving-body frame velocities u, v, and w using the transformation matrix which is determined from the quaternions e_0, e_1, e_2, and e_3.[19]

FUN3D has been linked to a 6-DOF library developed by the University of Alabama at Birmingham and Mississippi State University under the DOD PET program.[20] This library permits simulation of multiple moving bodies with compound forces and moments applied to each. It calculates rigid body motion under the influence of these external forces and moments using fourth-order Runge-Kutta temporal integration of Eq. 1.

III.A. Evaluation of Integration Schemes

The temporal integration scheme in the 6-DOF library is the fourth-order Runge-Kutta (RK4) explicit scheme. The RK4 scheme solves systems of first-order ordinary differential equations of the form $\{\dot{x}\} = f(t, \{x\})$. Equation 1 falls into this category. In the Runge-Kutta 4th-order (RK4) scheme, the state variables are not updated directly from time level t_n to time level t_{n+1}. Instead, they are updated in four intermediate steps. This Runge-Kutta scheme is popular because it reaches high-order accuracy without the need for storage of data from previous time steps. As an explicit scheme, an iterative process is not required, making it simple to implement in a computer code.

In the current application, however, the F and M terms in Eq. 1 present some difficulty. Ideally for computational efficiency, the 6-DOF library would receive forces and moments from the CFD solver once per time step, numerically integrate Eq. 1, and then return the updated values of the state variables to the solver again. This approach means that F and M, which are computed by FUN3D, cannot be updated during the intermediate time steps in the RK4 scheme, which certainly introduces error into the solution. Alternatively, for a proper implementation of the scheme, the flow solver would have to be called three additional times to recompute F and M for the intermediate steps. This approach is not desirable because it results in a computational cost four times that of the former approach.

To determine the influence of error in the solution of Eq. 1 when the RK4 scheme is used without updating F and M during the intermediate steps, a simple spring-mass test case was investigated. The mass was 40 kg and the spring constant was 1000 N/m. The simulation was initialized with the mass at rest and a stretched length of 1 m for the spring. The RK4 scheme was evaluated for this system by running a ten-second simulation with time step size ranging from 0.0001 seconds to 0.01 seconds in order to quantify numerical error and time-step convergence.

For an unforced spring-mass system with given initial conditions, the exact solution to the equation of motion is given by Eq. 2

$$x = C_1 \cos(\omega_n t) + C_2 \sin(\omega_n t) \tag{2}$$

where x is the stretched length of the spring, ω_n is the natural frequency, equal to $\sqrt{\frac{k}{m}}$, and C_1 and C_2 are constants that depend on the initial state of the system. Given $x(0) = 1$ and $\dot{x}(0) = 0$, it can easily be shown that $C_1 = 1$ and $C_2 = 0$. Thus, for this simple spring-mass system the solution to the equation of motion is

$$x = \cos(\omega_n t) \tag{3}$$

In assessing the accuracy of the scheme, the numerical output was matched with a curve fit of the following form

$$x = e^{\sigma t} \cos(\omega_n t) \tag{4}$$

where the term $e^{\sigma t}$ models the growth or decay of the amplitude in the solution. Since there is no physical damping in the problem, any damping in the numerical solution, either positive or negative, results from numerical error. The proximity of σ to 0 is indicative of the accuracy of the scheme. A non-negligible positive value of σ indicates instability of the system due to numerical error, and a negative value indicates numerical dissipation. The result for the RK4 scheme implementation in the 6-DOF library is shown in Fig. 1(a).

In Fig. 1(a), it is clear that there is significant error for the coarsest time step of 0.01 seconds. The growth rate σ decreases by an order of magnitude each time the time step decreases by an order of magnitude, so that with a very small time step of 0.0001 seconds the growth rate is on the order of 10^{-4}, which may be considered negligible. However, this time step size represents over 1200 steps per cycle, which is quite a large number even by CFD standards. For example, rotorcraft simulations on unstructured grids typically use 360 steps per revolution.[21] Therefore, the error introduced by this implementation of the RK4 scheme without force and moment updates at intermediate steps may be important in the coupled simulations.

With these results in mind for the test case, it is clear that a different time integration strategy is desirable for the 6-DOF equations of motion. Updating the forces and moments for the RK4 intermediate steps would significantly increase the computational cost of the simulation, so instead a different integration scheme was sought that does not require these intermediate steps. One such scheme is the Adams-Bashforth scheme.

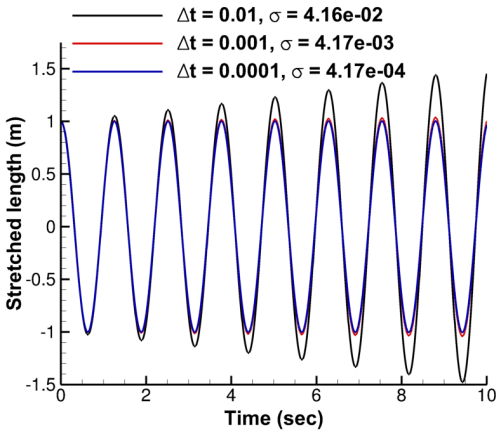

(a) Runge-Kutta scheme without force updates

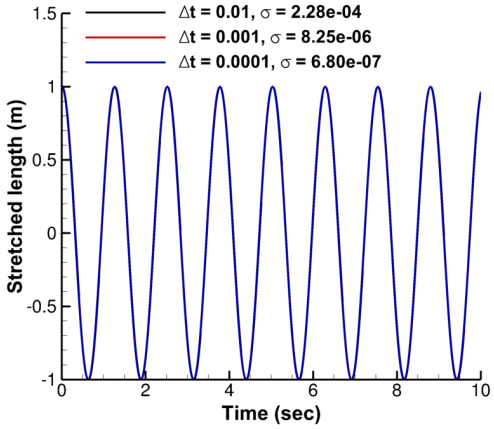

(b) Adams-Bashforth scheme

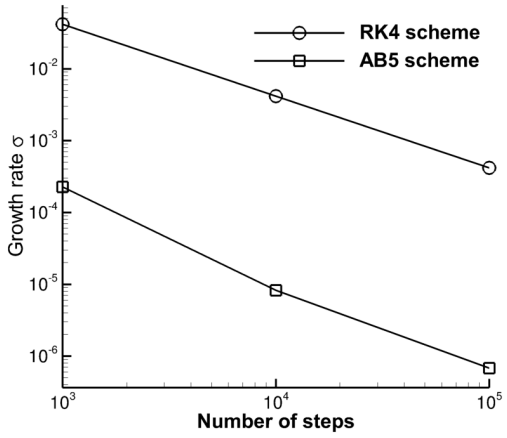

(c) Comparison of growth rate for Runge-Kutta and Adams-Bashforth

Figure 1: Exponential growth of spring amplitude in simulation of a spring-mass system for two different schemes

Like the RK4 scheme, the Adams-Bashforth scheme is also an explicit scheme and belongs to the family of linear multistep methods,[22] with the capability to achieve high accuracy up to fifth order. However, this scheme does not require any intermediate state updates like RK4. For the Adams-Bashforth scheme of order s, the state variables are updated from time t_n to t_{n+1} according to the following equation:

$$\{x\}_{n+1} = \{x\}_n + \Delta t \sum_{j=0}^{s-1} \alpha_{s,j} f\left(t_{n-j}, \{x\}_{n-j}\right) \tag{5}$$

The coefficients $\alpha_{s,j}$ may be determined via a Taylor series expansion of x and $f(t,x)$ terms in the equation and choosing $\alpha_{s,j}$ such that all terms above order s are canceled.[23] The coefficients up to order 5 are given in Table 1.[22]

Table 1: Coefficients for the Adams-Bashforth schemes

s	α_0	α_1	α_2	α_3	α_4
1	1	—	—	—	—
2	3/2	−1/2	—	—	—
3	23/12	−4/3	5/12	—	—
4	55/24	−59/24	37/24	−3/8	—
5	1901/720	−1387/360	109/30	−637/360	251/720

Equation 5 indicates that the Adams-Bashforth scheme of order s requires data for each of the thirteen state variables for the previous s time steps in order to update the system to time level $n+1$. This memory requirement is one downside of the Adams-Bashforth schemes in comparison with RK4. The Adams-Bashforth fifth-order scheme (AB5) was implemented into the 6-DOF library and tested for the same spring-mass case as presented for RK4. The results for the AB5 scheme are shown in Fig. 1(b). Figure 1(c) compares the exponential growth rate, σ, of the numerical solution on a log-log scale. From this figure it is apparent that the AB5 scheme performs much better in terms of numerical error than the RK4 scheme without intermediate force and moment updates. In fact, in this simple test case, σ was lower in magnitude for the AB5 scheme with a time step of 0.01 seconds than for the RK4 scheme with a time step two orders of magnitude smaller.

The AB5 scheme requires no calls to the flow solver during intermediate time steps, saving 75% the computational cost compared to a proper RK4 implementation for a coupled simulation. The downside to the AB5 scheme is the additional memory required to store the past state information f of Eq. 5. For the 6-DOF equations of motion being solved here, this amounts to 65 additional double precision floating point numbers per moving body, or 520 additional bytes. In the present effort, only one moving body is being simulated, so the memory cost is quite negligible. Based on these results, the AB5 scheme is used in all dynamic simulations of sling loads in this paper.

IV. Cable Modeling

Although FUN3D can simulate moving bodies in 6-DOF motion, only aerodynamic loads and loads that are known functions of time can be applied to the moving body. Thus, it was necessary to create a model of the cables which produce constraint forces and moments on the moving body. The cable model code passes these forces and moments to the 6-DOF library in addition to the aerodynamic forces and moments computed by the flow solver.

A simple model has been developed in which the cables produce spring-like and damper-like forces on the moving body. A similar approach was taken by Tyson et al.[24] The model is developed so that any number of cables may be attached to a moving body and to fixed points in space. The fixed points may be different for each cable, but note that this treatment precludes coupled simulation of helicopter and load dynamics because these points are fixed in inertial space. Consider Fig. 2, which provides an illustration of the cable modeling approach. In Fig. 2, a box is suspended by three cables. The tension produced by each cable i on the box is T_i. The tension on each cable acts in a direction along the vector from the fixed attachment point O_i in space to the attachment point P_i on the moving body. This direction is referred to as $\vec{e}_{ri}$. By setting the cable tension force in this direction, the assumption is made that the cable is straight.

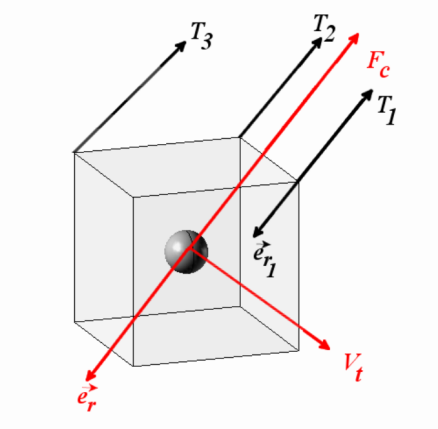

Figure 2: Model of a swinging box suspended by four cables in parallel

The sum of all three tension forces results in the overall cable force, $\vec{F}_c$, that is applied at the center of gravity (CG) of the moving body. For reference, the radial direction $\vec{e}_r$ and tangential component of velocity V_t are also shown for the moving body (though it is understood that the sum of forces F_c does not necessarily act along the vector $\vec{e}_r$). The tension force T_i of each cable is the result of two contributions, each acting in the negative radial direction for the cable,

$$\vec{T}_i = -\left(F_{si} + F_{di}\right)\vec{e}_{ri} \tag{6}$$

where F_{si} is a spring-like force, and F_{di} is a damper-like force. For a cable of length l_i, the magnitude of the spring-like force is a function of the distance between P_i and O_i. If this distance is d_i, then the magnitude of the spring-like force may be written

$$F_{si} = \begin{cases} k_i\left(d_i - l_i\right), & d_i \geq l_i \\ 0 & d_i < l_i \end{cases} \tag{7}$$

where k_i is the effective spring constant for the cable. Including a damping force is also important because it allows the tension force to reach a steady-state value without significant oscillation about some mean value, as would be the case if only the spring-like force were included. The magnitude of the damping force is given as

$$F_{di} = \begin{cases} c_i v_{ri}, & d_i \geq l_i \\ 0 & d_i < l_i \end{cases} \tag{8}$$

where c_i is the damping constant and v_{ri} is the velocity of the local attachment point P_i in the radial direction. Note that in Eqs. 7 and 8 it is possible for the cable to produce no force at all when $d_i < l_i$. This treatment allows a simple means to model a slack cable. The total constraint force $\vec{F}_c$ is just the sum of all the tensions:

$$\vec{F}_c = \sum_{i=1}^{N} \vec{T}_i \tag{9}$$

where N is the number of cables. To compute the moments, the only additional parameter required is the vector from the CG to points P_i, or $\vec{r}_{CGi}$. The total constraint moment applied at the CG is given as

$$\vec{M}_c = \sum_{i=1}^{N} \vec{r}_{CGi} \times \vec{T}_i \tag{10}$$

The parameters k and c may be determined in a number of ways. If the simulation is to be compared with an experiment, it may be possible to measure the effective spring and damping constants for the cables. The spring constant is related to the modulus of elasticity for the material and can be determined by stretching

the spring with a known applied force and measuring the strain. The damping constant can be more difficult to determine experimentally. In a less precise approach, the spring constant may be estimated by providing a maximum desired stretch for some condition (say, in a pendulum swinging motion) and determining the spring constant necessary to achieve that motion. The damping constant, in turn, can be set to a value that is sufficiently large to result in an overdamped system for the mass-spring-damper system. Such an approach would be appropriate if the cables are quite stiff and not expected to stretch and unstretch in an oscillatory fashion. However, a cable that is very stiff (with a large spring constant) may result in numerical instability if the time step is too large.

V. Simulations and Results

V.A. Static Simulations

Simulation of bluff bodies in turbulent flow in CFD is challenging even without dynamics included, involving separation, reattachment, and unsteady shedding of the turbulent shear layer.[11] Therefore, it is important to first validate the flow solver and simulation procedures against static data before moving on to dynamic cases.

CFD simulations were performed to compare with experimental data for a box configuration. Experimental data used for the correlation was carried out in the 9 x 7 ft. John J. Harper wind tunnel at the School of Aerospace Engineering of Georgia Institute of Technology.[10,25] The box configuration is a $1/11^{\text{th}}$-scale model of Container Express (CONEX) cargo container.[4] The dimensions and inertial parameters (the latter of which are important for dynamic simulations) of the box are given in Table 2.

Table 2: Dimensions and inertial parameters for box

Length (m)	0.23368	Mass (kg)	1.490
Width (m)	0.16764	I_{xx} (10^{-3} kgm^2)	11.04
Height (m)	0.17145	I_{yy} (10^{-3} kgm^2)	7.77
		I_{zz} (10^{-3} kgm^2)	10.49

The static simulations were intended to demonstrate many of the complex unsteady aerodynamic effects which occur in the dynamic cases as well, including separation, reattachment, and unsteady turbulent vortex shedding. Static simulations were performed for the box at a single pitch angle of 0 degrees with yaw angles varying from 0 to 90 degrees. The experiments were performed at a tunnel speed of 35 mph, resulting in a Reynolds number of 215,000 based on the average of length and width.

An overset mesh approach is used with a near-body grid for the box placed inside a background grid representing the Harper wind tunnel. The overset grid has 3.2 million vertices. The near-body grid is mixed element with prismatic elements in the boundary layer. The composite grid is comprised of 58% tetrahedral elements and 42% prismatic hexahedral elements. Face angles in the grid range from 8.7° to 160.9° with a mean of 76.6° and standard deviation of 21.1°. For accurate resolution of the turbulent boundary layer, 35 cells were used in the normal direction with a dimensionless wall distance, y^+, less than 1 on the surface. Boundary layer parameters similar to these have been used successfully in previous studies of unsteady, separated bluff-body flows.[26] A side view of the grid and boundary layer are shown in Fig. 3. In this figure, the box is placed at the $\beta = 0$ orientation.

Static simulations were performed in time-accurate mode to capture the unsteady bluff-body vortex shedding. A hybrid RANS-LES turbulence model was used to resolve large eddies and turbulent fluctuations in the wake while modeling boundary layer turbulence. This model has been shown to give good predictions in bluff-body simulations in the past.[15,16] Time averaged coefficients of drag, side force, and yaw moment are presented in Fig. 4 for the simulations along with two sets of experimental data. Force coefficients are normalized by the average of the front and side areas, since during the β sweep from 0 to 90 degrees the front and side faces switch positions. Yaw moments are measured about the center of the box and are non-dimensionalized by the same area and by the average of box length and width as the reference length dimension. The time-accurate CFD simulations were run long enough that the forces and moments could be averaged over several cycles of vortex shedding.

Overall, correlation between CFD and experiment in the static simulations is quite good. There is some

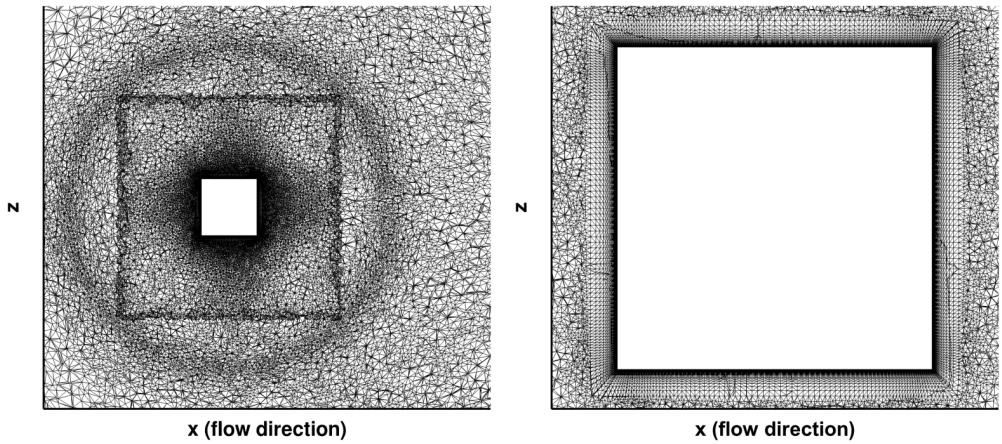

(a) Side view (x-z plane) (b) Close-up of boundary layer

Figure 3: Grid for box simulations (at $\beta = 0$ degrees)

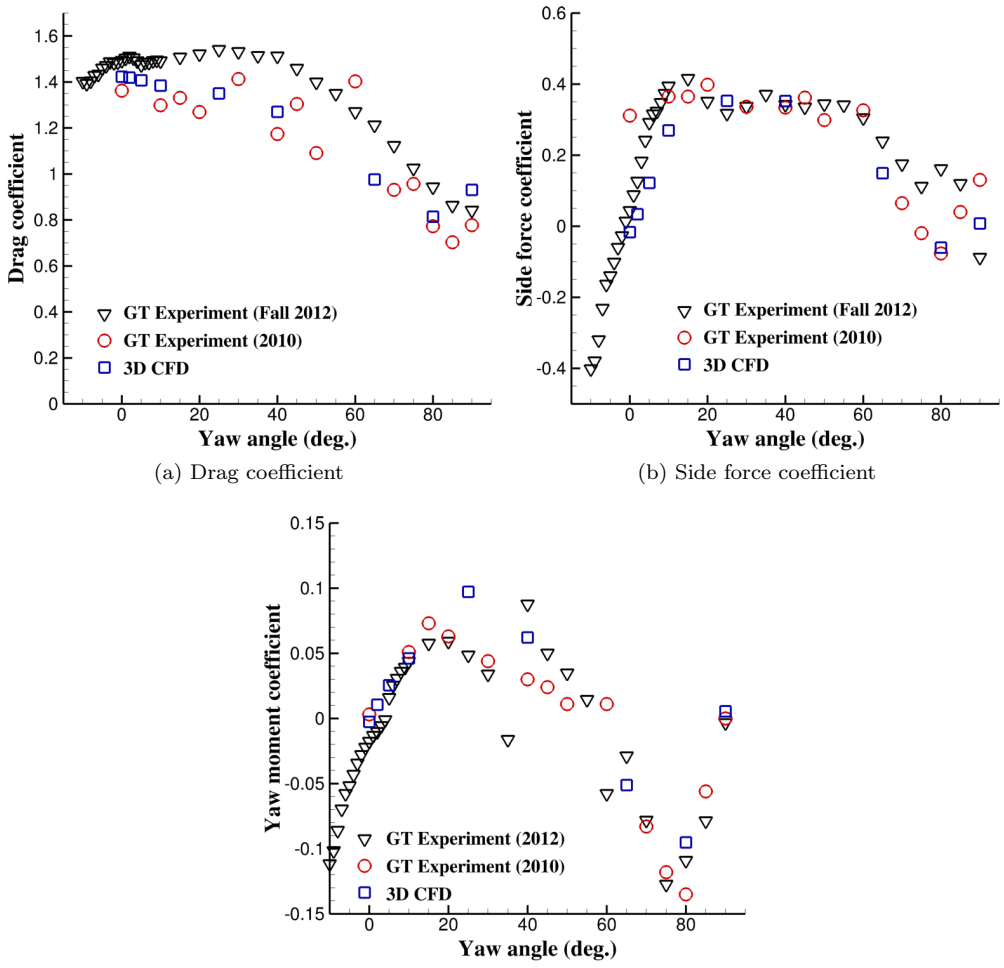

(a) Drag coefficient

(b) Side force coefficient

(c) Yaw moment coefficient

Figure 4: Mean force and moment coefficients for box at $Re = 215,000$ in a sweep of yaw angle. Experimental data from Mantri et al.[10,25]

scatter in the experimental data, particularly in the 2010 drag data and 2012 experimental yaw moment data. CFD agrees well with both sets of experimental drag data at 0 degrees and near 90 degrees, but at 90 degrees the CFD prediction is slightly higher than experiment. At mid-range yaw angles, the CFD prediction is very close to the 2010 experimental data, though there is scatter in the data there. The CFD prediction and both sets of experimental data agree well over most of the sweep for side force and yaw moment. In the side force, there are some discrepencies near $\beta = 90$, and here the CFD data correlates more closely with the 2010 experimental data. The CFD data predicts a somewhat higher peak in yaw moment than the experimental data in the lower half of the β sweep but somewhat lower (in magnitude) peak at the higher end. Despite these small differences, however, the CFD data is generally near the center of the two experimental data sets, so confidence in the CFD methodology is high. The data also compares well with prior work by Theron et al.[9]

V.B. Dynamic Simulations

V.B.1. Experimental validation

A number of dynamic experiments were previously performed in the John Harper tunnel using the $1/11^{\text{th}}$ scale CONEX box model.[10] Flow velocities in the tunnel at which measurements were taken ranged from 10 to 45 mph, corresponding to a Reynolds number of 85,000 to 390,000 based on the average side length. In each case, the box model was suspended from the top of the tunnel by four cables attached to the top corners of the box. Wind tunnel tests did not account for any helicopter dynamics (the sling load was attached to the ceiling of the wind tunnel) or rotor wake interactions on the sling load. The mount at the top of the tunnel was gimballed so that rotation could occur freely in any direction. The dynamic experiments started from rest with the narrow side of the box (corresponding to the width dimension) facing forward and the tunnel off. The flow velocity was slowly increased in increments of 5 mph, and the mean trailing angle was measured after allowing enough time for flow transients from the change in tunnel velocity to die out. Four different box models were tested, with varying moment of inertia, but for comparison with CFD only the model with the greatest moment of inertia was considered. The mass and moments of inertia for this configuration are given in Table 2.

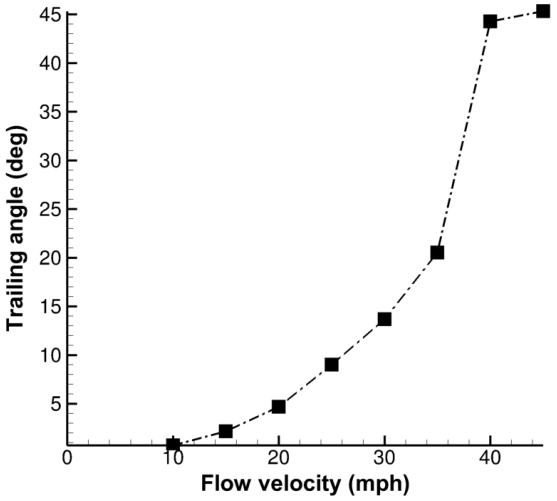

Figure 5: GT experimental data for mean trailing angle for the box model as a function of tunnel velocity[10]

Figure 5 shows the results from the wind tunnel tests. Initially, the trailing angle increases in a manner roughly proportional to the square of tunnel velocity. Above 35 mph, a sudden increase in trailing angle occurs. This sudden increase in trailing angle occurs because the yaw oscillations of the box have become large enough that the narrow side is no longer facing forward. Instead the broad side faces forward, causing a sharp increase in drag and trailing angle. CFD simulations in this paper attempt to correlate with the mean trailing angle data of Fig. 5 and also to capture the transition from narrow-side-forward to broad-side-forward (hereafter referred to as NS-BS transition).

V.B.2. 25 mph simulation

Initial simulations were performed at 25 and 40 mph for comparison with experimental data. The simulations used the same overset grid as in the static simulations (Fig. 3). The background grid is a model of the test section of the tunnel, and the overset grid has 3.2 million nodes. These two flow speeds were selected because of their differing NS-BS transition behavior in the experimental data.

In the first cases, the simulations were initialized with the box hanging at rest directly below the attachment point of the cables at the top of the tunnel. The flow was initialized in two steps. First, the solver was run in steady mode to remove flow transients, and subsequently it was run unsteady for 500 steps

with the box held static to allow the unsteady separated wake to develop. This procedure allows an accurate representation of the initial flow field so that unnecessary errors are not introduced into the dynamic simulation.

The 25 mph simulation ran for over 20,000 time steps, equating to 6.24 seconds of physical time. The simulation required roughly 18 hours per 1000 steps on 64 processors, highlighting the expense of dynamic bluff body simulations in CFD. Figure 6 gives the euler angles and angular rates for the box during the simulation.

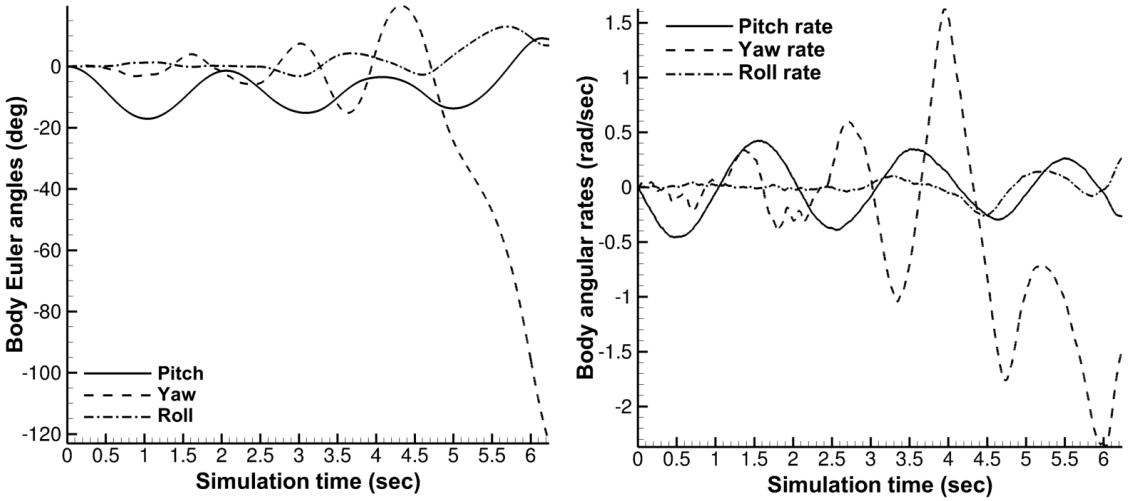

(a) Euler angles (b) Angular rates about body axes

Figure 6: Results of the initial 25 mph simulation

For the first 5 seconds of the simulation, the box undergoes pitch oscillations which are both caused and damped primarily by drag. The damped nature of the oscillations indicates that a periodic "steady-state" solution is being reached for the pitch angle. However, the aerodynamics and dynamics are highly coupled and nonlinear, and while the pitching motion is being damped by drag, there is also a yawing motion that grows with time. After 5 seconds, the yaw angle increases to the point that the box undergoes NS-BS transition, disrupting the periodic pitch oscillation. Note that the rapid departure of yaw angle during NS-BS transition is not indicative of numerical instability, as flow residuals maintain good convergence during this dynamic behavior.

The small mean trailing angle of 9 degrees for the 25 mph test in Fig. 5 indicates that in the experimental this NS-BS did not take place. This discrepancy needs to be investigated further. Considering the relatively simple model of the cables used in the simulation, it is possible that discrepancies in the dynamics are caused by the cable model. For example, if there is some drag in the experimental gimbal mount, some yaw damping would be present whereas there is none in the cable model used in simulation. Other possible causes, which are investigated in this paper, include differences in starting condition or a need for grid refinement in CFD.

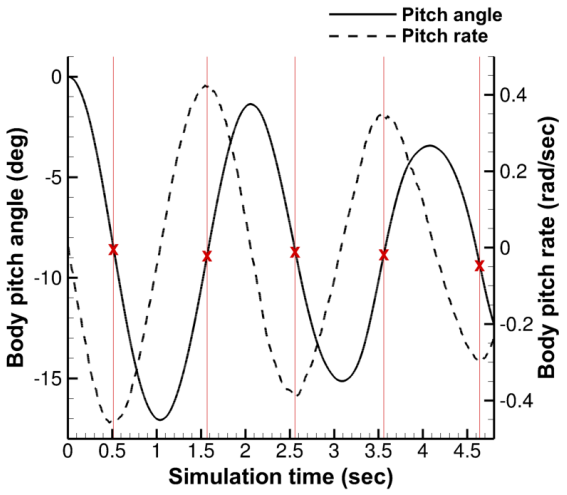

Figure 7: Prediction of mean trailing angle

Despite the difference in NS-BS transition behavior observed in the dynamics, the pitch oscillations before transition occurs are nonetheless useful for predicting the mean trailing angle if transition had not occurred. During the first 5 seconds of the simulation, the box undergoes two and a half pitch oscillations, shown in Fig. 7. This figure overlays the pitch angle and pitch rate on the same plot. Provided

no NS-BS transition had occurred, it would be expected that the mean trailing angle would be close to the each angle at which the slope of the pitch rate is 0 in these first two and a half oscillations, because the net force in the tangential direction is 0 at these points. The predicted mean trailing angle using this approach is 8.8 degrees, which is remarkably consistent with the experimental result of 9 degrees.

V.B.3. 40 mph simulation

The 25 mph simulation demonstrates that CFD can accurately predict the mean trailing angle of the sling load. To further investigate the NS-BS transition phenomenon, a 40 mph simulation was also performed. Figure 8 gives the body angles and angular rates for the 40 mph simulation. Major differences in this simulation compared with the 25 mph case include the magnitude of the pitch angle during the initial swing, which is about 40 degrees for this case compared with 17 degrees for the other, and that the yaw and roll amplitudes become large much earlier in the simulation. In this simulation NS-BS transition occurs after 2.5 seconds, whereas in the 25 mph simulation it occured after 5 seconds. This is expected, because the aerodynamic moments responsible for the transition behavior are greater in magnitude for the 40 mph case. This transition was also observed in the experimental tests for the 40 mph case, but not for the 25 mph case.

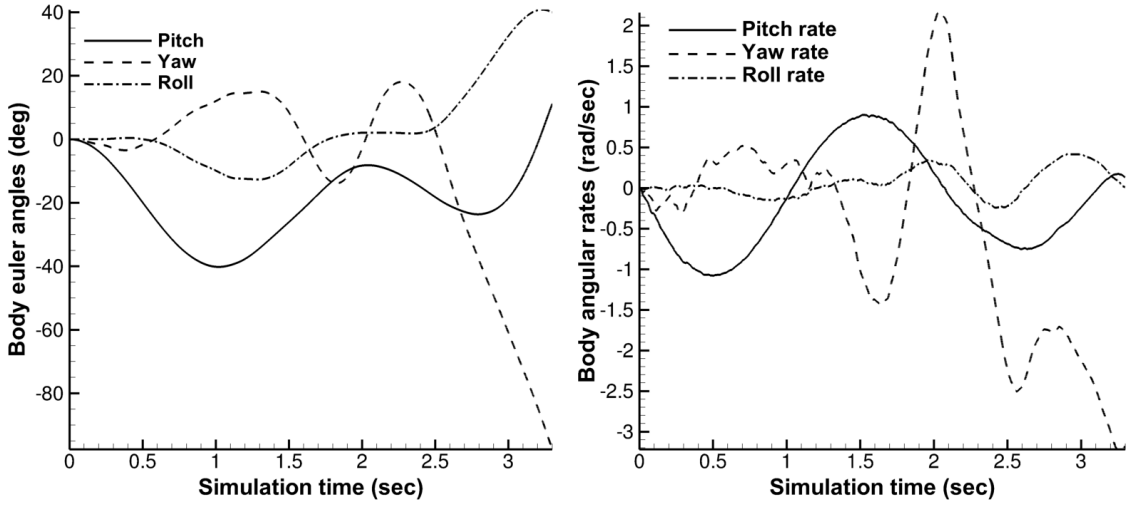

(a) Euler angles (b) Angular rates about body axes

Figure 8: Results of the initial 40 mph simulation

In the 40 mph case, the NS-BS transition occurs after less than two pitch cycles. The mean trailing angle before transition occurs is about 20 degrees; however, this cannot be compared with the experimental data of Fig. 5 because at 40 mph the trailing angle reported is for post NS-BS transition. Due to the cost of the simulations, the 40 mph case was not run for long following the NS-BS transition. In the future if correlation of the mean trailing angle is desired for the 40 mph case, the simulation should be initialized with the broad side facing forward and at an initial trailing angle close to that recorded in experiment. This type of initialization allows the final mean trailing angle to be captured without requiring as long a simulation.

Although NS-BS transition behavior was encountered in the 25 mph simulation but not in experiment, the time required for this behavior to occur in the two simulations is encouraging because it highlights the trend seen in experiment. Namely, the NS-BS transition occurs more quickly at higher flow speeds. The fact that this trend is captured in simulation also suggests that some damping may be needed in the cable model to accurately represent the real attachment.

A significant benefit of numerical simulation is the wealth of data that is readily available without the need for expensive instrumentation. This data can provide valuable insight into the flow physics. As an example, during the 25 mph simulation, pressure distributions and flow field samples were saved periodically. Figure 9 shows a side view of the box and grid colored by contours of vorticity magnitude at various steps in the simulation, which highlights the highly separated and turbulent nature of the flow. Of particular interest is the difference in the shear layer behavior in the three snapshots. Initially, both the top and bottom surfaces of the box experience fully separated flow. After 1700 steps, the boundary layers are still

fully separated on the top and bottom surfaces, but the shear layer is moving closer to the top surface. After 3450 steps, the shear layer on the top surface has reattached, and a separation bubble has formed. Figure 10 shows the pressure distributions on the top and bottom surfaces of the box at the same points in the simulation, revealing regions of attached flow, separation, and reattachment. These complexities in flow physics can greatly influence the forces acting on the box and make simplified aerodynamic modeling particularly challenging.[2,11,27]

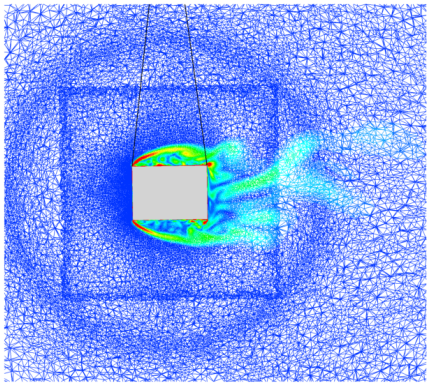

(a) After 500 steps (0.15 seconds)

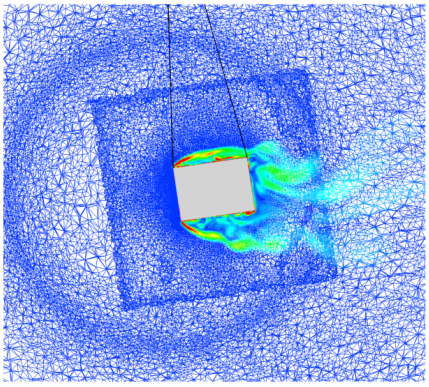

(b) After 1700 steps (0.51 seconds)

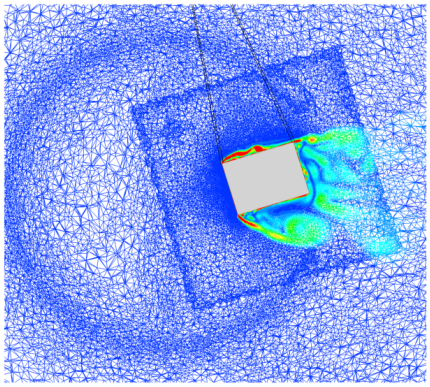

(c) After 3450 steps (1.04 seconds)

Figure 9: x-z slice of the flow field colored by vorticity magnitude

V.B.4. Initial conditions

In order to minimize pitch oscillations and better approximate the conditions in the wind tunnel, the 25 mph case was re-evaluated with new initial conditions. Instead of hanging at rest directly below the cable attachment point at the top of the tunnel, the estimate of the final mean trailing angle from the previous simulation was used as the initial position.

In addition to being more representative of the wind tunnel tests, it is hypothesized that the initial conditions may have an impact on the NS-BS transition behavior. The initial conditions used for the original 25 mph and 40 mph simulations resulted in significant pitch oscillations, as seen in Figs. 6 and 8. The pitch oscillations are especially large in the 40 mph simulation. Figure 8(b) shows that the maximum magnitude of pitch rate is around 1.1 rad/sec, which occurs during the first upswing. The body velocity

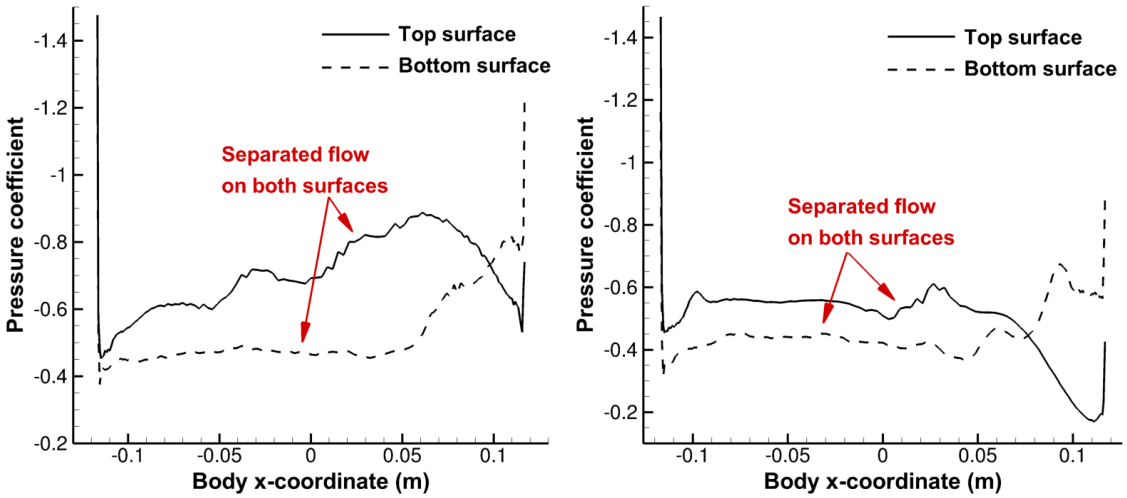

(a) After 500 steps (0.15 seconds)

(b) After 1700 steps (0.51 seconds)

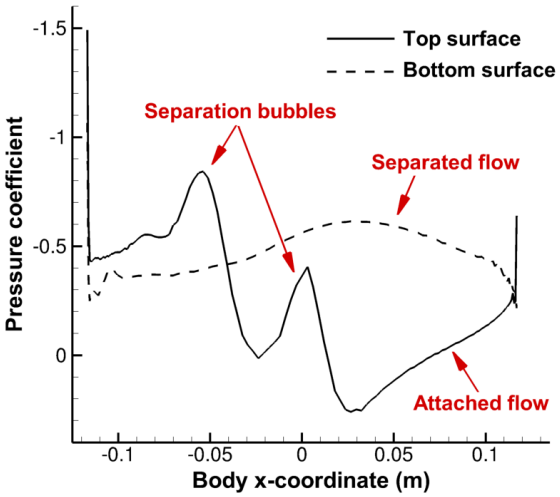

(c) After 3450 steps (1.04 seconds)

Figure 10: Surface pressures revealing regions of separated and attached flow

corresponding to this point in time is 1.14 m/s, or about 6.5% the upstream velocity of the flow. Considering that the aerodynamic forces and moments are proportional to the square of the total air velocity seen by the box, a 6.5% increase in relative velocity corresponds to a 13.5% increase in the forces and moments. Therefore, it is expected that the large swinging amplitudes in the initial simulation may cause the NS-BS transition to occur more quickly than in a simulation with less extreme pitch oscillations.

Figure 11 shows the results of a 25 mph simulation with new initial conditions. In this case, the box starts from rest hanging with an 8.8° trailing angle. The solution is initialized in the same manner as the original simulations; first, a steady-state simulation is performed for 500 iterations in order to remove transients arising from the initial flow field. Next, a time-accurate simulation is performed while the box remains static to allow the unsteady wake to be set up. The dynamic simulation begins after this initialization procedure.

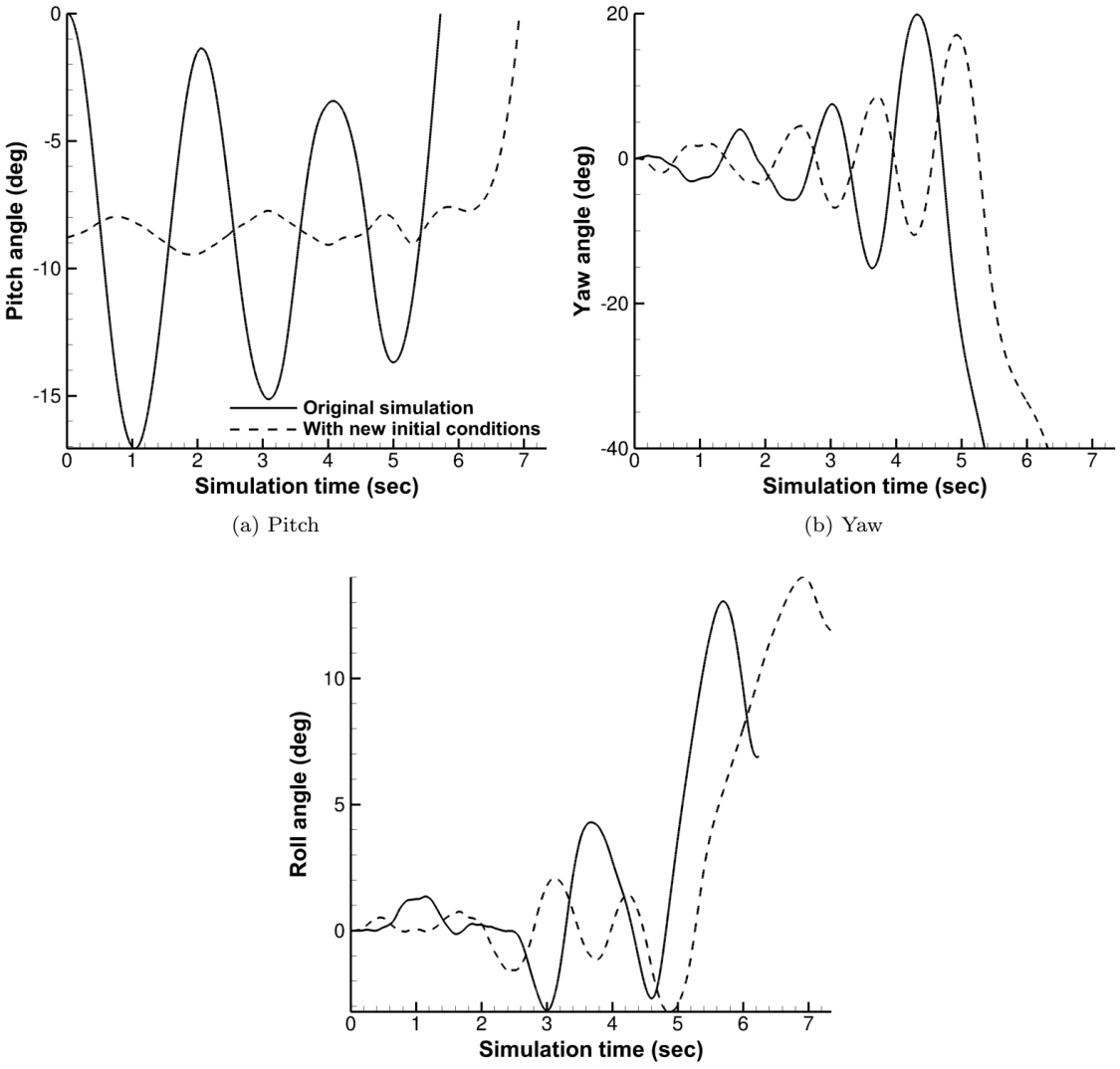

(a) Pitch

(b) Yaw

(c) Roll

Figure 11: Comparison of Euler angles for the original 25 mph simulation and a 25 mph simulation with modified initial conditions

Figure 11(a) shows the pitch angle for the original simulation and the simulation with new initial conditions. The most obvious difference in this figure is the drastic difference in amplitude of pitch oscillations. As expected, using the expected mean trailing angle as the initial trailing angle results in only small pitch oscillations about the mean. In this case, the oscillation magnitude is around 1 degree in either direction. The period of pitch oscillations is also very similar to the initial simulation, but the phase is different by 180°. In the case with new initial conditions, the box first swings down instead of up, giving rise to the

phase differnce.

Figures 11(b) and (c) compare the yaw and roll angles, respectively, for the two simulations. In both cases, behavior similar to that of the pitch oscillations is seen. The magnitudes of yaw and roll oscillations are smaller for the case with new initial conditions up until NS-BS transition. This result is expected, because the smaller pitch oscillations result in smaller dynamic pressures and thus smaller magnitudes of forces and moments. As was the case for the pitch angle, the yaw and roll oscillations exhibit a phase shift of 180° relative the original simulation.

In addition to the reduced oscillation magnitudes and phase differences compared to the original simulation, with the new initial conditions NS-BS transition is delayed. Figure 11(b) shows that the transition occurs one half cycle later for the simulation with new initial conditions. This result supports the hypothesis which motivated the simulation. The new initial conditions did not completely eliminate NS-BS transition. However, the study does demonstrate that in a nonlinear system with coupled degrees of freedom, details such as initial conditions can have an effect on dynamics and stability.

V.B.5. Grid adaptation

Due to the expense of unsteady bluff body simulations in CFD, a full grid independence study is not practical. Instead, for the simulations in Sections V.B.2–V.B.4 the same grid was used which gave good results in the static simulations. FUN3D has the capability to perform adaptive grid refinement based on flow features.[28,29] Grid adaptation is a powerful way to refine the grid so that points are concentrated in the regions where they are needed while coarsening the grid elsewhere, resulting in an accurate solution with high grid efficiency. This approach has been routinely applied to rotorcraft and wind turbine simulations with success.[30–32]

This capability is present in FUN3D for steady or unsteady simulations on single or overset grids. A metric-based approach is taken, which builds up information about flow conditions throughout the grid during a portion of the simulation. The metric-based approach requires specification of a flow field indicator, which may be vorticity magnitude, pressure gradient, velocity gradients, or other quantities. After the metric is constructed during the simulation, the grid is refined based on the local value of this metric. For this study vorticity magnitude was used as the indicator. This indicator has been used successfully in other dynamic simulations of bluff bodies.[33]

The time window to build the metric in a dynamic simulation should be long enough so that the adapted grid is refined everywhere needed. In the present case, the time window was constructed for the interval between 1.9 and 3.1 seconds in the simulation with new initial conditions (Fig. 11). This time interval brackets the downward swing of the box during its second pitch oscillation cycle and also contains a full cycle of yaw oscillation. After building the time-dependent metric, the near body and background grids are adapted based on this metric information. Figure 12 shows the top view of the baseline and adapted grid. The baseline grid has 3.2 million nodes, and after adaptation that number increases to 5.3 million. Figure 12 shows that the grid has been refined in the separated shear layer region and in the wake. Elsewhere in the grid, there are some differences between the two but the overall grid density remains similar.

Starting with the adapted grid, the simulation with new initial conditions was re-run to assess the effect of grid adaptation on the dynamics. Figure 13 shows the pitch and yaw angles compared for the baseline and adapted grid simulations. There are several notable differences in the pitch angle for the two simulations. First, the adapted grid simulation has a longer initial downswing after release and establishes a smaller mean trailing angle before NS-BS transition occurs. The longer downswing also introduces a phase difference in the pitch oscillations between the two simulations.

Figure 13(b) shows that the yaw oscillations are initially smaller for the adapted case, but that they eventually grow larger. There is also a phase difference in yaw between the two cases which tends to grow with time, indicating that the frequency of yaw oscillations is greater for the adapted case than the baseline case. The eventually-larger yaw oscillations result in an earlier NS-BS transition than in the baseline case.

Even though the adapted-grid case resulted in NS-BS transition sooner than the baseline case, the initial yaw oscillations are smaller in magnitude, indicating that the initial yaw moment is also smaller. The smaller initial yaw moments indicate that under some conditions grid adaptation may help delay NS-BS transition behavior for the 25 mph case to better correlate with the experimental result. To investigate this possibility further, coupling interactions between the various degrees of freedom need to be analyzed in detail. The initial conditions are also shown to have a significant effect on the dynamics of the system, so in future comparisons between experiment and CFD the initial conditions should be carefully synchronized between the two.

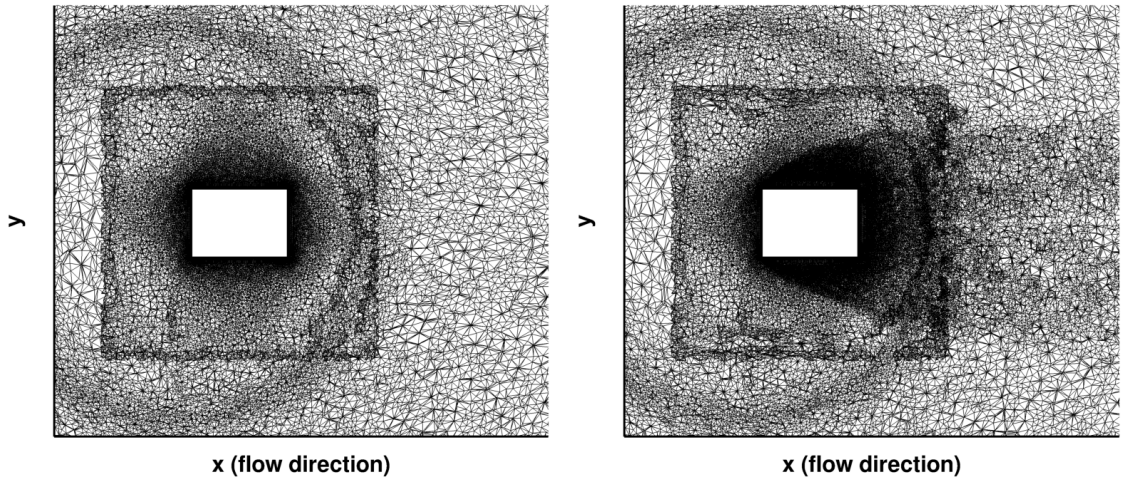

(a) Baseline grid (b) Adapted grid

Figure 12: Top view grid in the vicinity of the box for the baseline and adapted grids

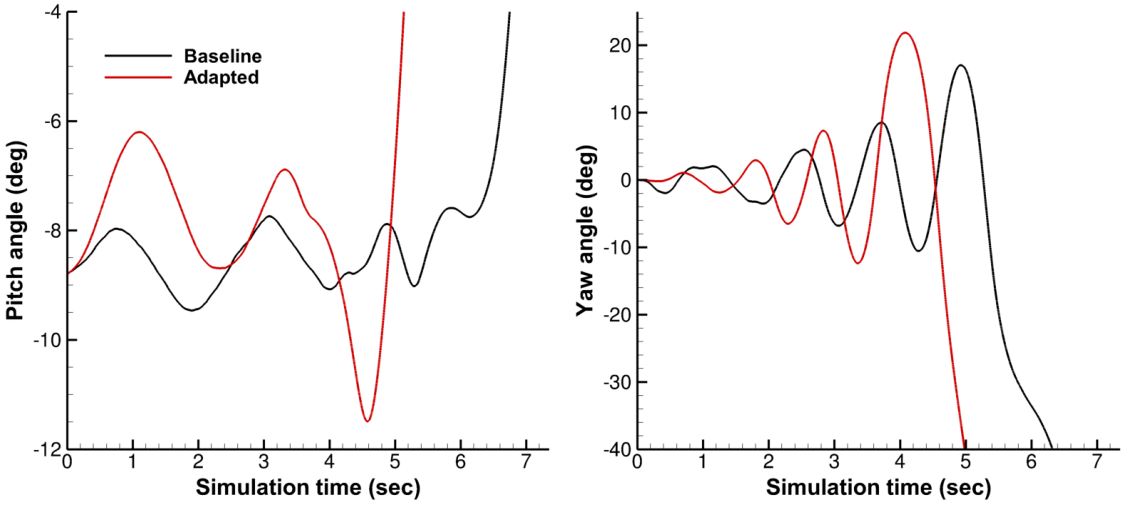

(a) Pitch angle (b) Yaw angle

Figure 13: Pitch and yaw angles for the baseline and and adapted 25 mph simulations

VI. Conclusions

In this paper, the Navier-Stokes equations and rigid body equations of motion are coupled to simulate the dynamics of sling loads. Two different time integration implementations are evaluated for the rigid body equations of motion, and the Adams-Bashforth fifth-order scheme is used for dynamic simulations because of its accuracy and benefits in coupled simulations with respect to computational expense. For simulation of sling loads, constraint forces and moments are computed by modeling the cables with a spring-damper representation.

Before performing any dynamic simulations, the CFD solver was first validated against wind tunnel data for the box geometry over a wide range of yaw angles, showing good correlation. Dynamic simulations were then performed at 25 mph and 40 mph and compared with wind tunnel results. Key results of the dynamic simulations include:

- The mean trailing angle observed in experiment is accurately captured by CFD for the 25 mph case. For the 40 mph case, the simulation would need to be run further beyond NS-BS transition or restarted with initial conditions close to what is expected for the final mean trailing angle in order to assess the accuracy of the mean trailing angle prediction.
- NS-BS transition behavior is observed in both the 25 and 40 mph simulations. In experiment, this behavior was seen at 40 mph but not 25 mph. In simulation, NS-BS transition occurs more quickly in the 40 mph simulation than the 25 mph simulation.
- Using initial conditions close to the final mean trailing angle results in significantly smaller pitch oscillations and longer time to NS-BS transition, indicating that initial conditions can have a significant effect on the dynamics of a coupled nonlinear system. Better correlation between simulation and experiment is achieved when the initial conditions are closely matched.
- Grid adaptation results in smaller initial yaw moment magnitude but eventually larger yaw moments and faster NS-BS transition for the 25 mph case.
- Improvements to the cable model are suggested to improve correlation between experiment and CFD. In particular, yaw damping may be required in the cable model.

Based on the results of this study, several items need to be investigated in future work. Measurements of the yaw damping in the experimental cable attachment should be taken and applied in the CFD model. The coupling between various degrees of freedom should be investigated; specifically, the effect of this coupling on yaw moment and other forces and moments should be determined. Further validation with experiment should be performed to ensure that inclusion of proper yaw damping removes the NS-BS transition behavior in the 25 mph case. In the longer term, modes and causes of dynamic instability in sling load operations can be investigated using this Navier-Stokes-based dynamic simulation framework, and this work will help to reduce the cost required for sling loads operational clearance.

Acknowledgements

The authors would like to recognize and thank the experimental group in the Aerospace Engineering department at The Georgia Institute of Technology for generating the experimental data used for validation in this work, especially Narayanan Komerath, Sumant Sharma, Ranjit Mantri, and Vrishank Raghav. The authors would also like to thank Ross Cooper for creating the background grid used in the simulations. This work is supported by funding from the Army and the Vertical Lift Research Center of Excellence at the Georgia Institute of Technology.

References

[1]Raz, R., Rosen, A., Cicolani, L. S., Lusardi, J., Gassaway, B., and Thompson, T., "Using Wind Tunnel Tests for Slung Loads Clearance," *Proceedings of the 67th American Helicopter Society Annual Forum*, Virginia Beach, Virginia, May 3–5, 2011.

[2]Greenwell, D., "Modelling of Static Aerodynamics of Helicopter Underslung Loads," *The Aeronautical Journal*, Vol. 115, No. 1166, April 2011, pp. 201–219.

[3]Wilson, G. J. and Rothman, N. N., "Evaluation, Development, and Advantages of the Helicopter Tandem Dual Cargo Hook System," *AGARD Conference Proceedings, No. 121 on Advanced Rotorcraft*, Paris, France, February 1973.

[4]Raz, R., Rosen, A., Carmeli, A., Lusardi, J., Cicolani, L. S., and Robinson, L. D., "Wind Tunnel and Flight Evaluation of Passive Stabilization of a Cargo Container Slung Load," *Journal of the American Helicopter Society*, Vol. 55, No. 3, July 2010.

[5]Cicolani, L. S., Raz, R., Rosen, A., Gordon, R., Cone, A., Theron, J. N., Lusardi, J., Tischler, M., and Robinson, M. D., "Flight Test, Simulation and Passive Stabilization of a Cargo Container Slung Load in Forward Flight," *Proceedings of the 63rd American Helicopter Society Annual Forum*, Virginia Beach, VA, May 1–3, 2007.

[6]Cicolani, L. and da Silva, J, G., "Unsteady Aerodynamic Model of a Cargo Container for Slung-Load," *The Aeronautical Journal*, Vol. 108, No. 1085, July 2004, pp. 357–368.

[7]Cicolani, L. S., Cone, A., Theron, J., Robinson, L. D., Lusardi, J., Tischler, M. B., Rosen, A., and Raz, R., "Flight Test and Simulation of a Cargo Container Slung Load in Forward Flight," *Journal of the American Helicopter Society*, Vol. 54, No. 3, July 2009, pp. 1–18.

[8]Theron, J. N., Duque, E. P. N., Cicolani, L., and Halsey, R., "Three-Dimensional Computational Fluid Dynamics Investigation of a Spinning Helicopter Slung Load," *31st European Rotorcraft Forum*, Florence, Italy, September 13–15, 2005.

[9]Theron, J. N., Gordon, R., Rosen, A., Cicolani, L., Duque, E. P., and Halsey, R. H., "Simulation of Helicopter Slung Load Aerodynamics: Wind Tunnel Validation of Two Computational Fluid Dynamics Codes," *AIAA 36th Fluid Dynamics Conference and Exhibit*, No. AIAA-2006-3374, San Francisco, CA, June 5–8, 2006, pp. 1–14.

[10]Mantri, R., Raghav, V., Komerath, N., and Smith, M. J., "Stability Prediction of Sling Load Dynamics Using Wind Tunnel Models," *Proceedings of the 67th American Helicopter Society Annual Forum*, Virginia Beach, Virginia, May 3–5, 2011.

[11]Prosser, D. T. and Smith, M. J., "Characterization of Flow Around Rectangular Bluff Bodies at Angle of Attack," .

[12]Bonhaus, D., *An Upwind Multigrid Method For Solving Viscous Flows On Unstructured Triangular Meshes*, Master's thesis, George Washington University, 1993.

[13]Anderson, W., Rausch, R., and Bonhaus, D., "Implicit/Multigrid Algorithms for Incompressible Turbulent Flows on Unstructured Grids," *Journal of Computational Physics*, Vol. 128, No. 2, 1996, pp. 391–408.

[14]Shenoy, R. and Smith, M., "Unstructured Overset Grid Adaptation for Rotorcraft Aerodynamic Interactions," *Proceedings of the 67th American Helicopter Society Annual Forum*, Virginia Beach, Virginia, May 3–5 2011.

[15]Lynch, C. and Smith, M., "Hybrid RANS-LES Turbulence Models on Unstructured Grids," *Proceedings of the 38th AIAA Fluid Dynamics Conference and Exhibit*, Seattle, WA, June 2008.

[16]Sánchez-Rocha, M. and Menon, S., "The Compressible Hybrid RANS/LES Formulation Using an Additive Operator," *Journal of Computational Physics*, Vol. 228, No. 6, April 2009, pp. 2037–2062.

[17]Noack, R., "DiRTlib: A Library to Add an Overset Capability to Your Flow Solver," *17th Computational Fluid Dynamics Conference*, American Institute of Aeronautics and Astronautics, Toronto, Ontario, June 2005.

[18]Noack, R., "SUGGAR: A General Capability for Moving Body Overset Grid Assembly," *17th Computational Fluid Dynamics Conference*, American Institute of Aeronautics and Astronautics, Toronto, Ontario, June 2005.

[19]Phillips, W., Hailey, C., and Gebert, G., "A Review of Attitude Kinematics for Aircraft Flight Simulation," *AIAA Modeling and Simulation Technologies Conference and Exhibit*, No. AIAA-2000-4302, Denver, Colorado, August 14–17, 2000.

[20]Biedron, B., "FUN3D Training Workshop Session 9: Overset and 6-DOF Simulations," `http://fun3d.larc.nasa.gov`, July 27–28, 2010.

[21]Biedron, R. T. and Lee-Rausch, E. M., "Rotor Airloads Prediction Using Unstructured Meshes and Loose CFD/CSD Coupling," *Proceedings of the 26th AIAA Applied Aerodynamics Conference*, No. AIAA 2008-7341, Honolulu, Hawaii, 2008.

[22]Hairer, E., Nørsett, S. P., and Wanner, G., *Solving Ordinary Differential Equations I: Nonstiff Problems*, Springer-Verlag, Berlin, 2nd ed., 1993.

[23]Durran, D. R., "The Third-Order Adams-Bashforth Method: An Attractive Alternative to Leapfrog Time Differencing," *Monthly Weather Review*, Vol. 119, No. 3, March 1991, pp. 702–720.

[24]Tyson, P. H., Cicolani, L. S., Tischler, M. B., Rosen, A., Levine, D., and Dearing, M., "Simulation Prediction and Flight Validation of UH-60A Black Hawk Slung-Load Characteristics," *Proceedings of the 55th American Helicopter Society Annual Forum*, Montral, Canada, May 25–27 1999.

[25]Mantri, R., Raghav, V., Komerath, N., and Smith, M. J., "Study of Factors Driving Pitch, Roll, and Yaw Coupling in Bluff Body Aerodynamics," *AIAA 41st Fluid Dynamics Conference and Exhibit*, No. AIAA-2011-3445, Honolulu, Hawaii, June 27–30, 2011.

[26]Smith, M. J., Liggett, N. D., and Koukol, B. C., "Aerodynamics of Airfoils at High and Reverse Angles of Attack," *AIAA Journal of Aircraft*, Vol. 48, No. 6, November–December 2011, pp. 2012–2023.

[27]Norberg, C., "Flow around Rectangular Cylinders: Pressure Forces and Wake Frequencies," *Journal of Wind Engineering and Industrial Aerodynamics*, Vol. 49, No. 1–3, December 1993, pp. 187–196.

[28]Park, M. and Darmofal, D., "Parallel Anisotropic Tetrahedral Adaptation," *AIAA 46th Aerospace Sciences Meeting and Exhibit*, No. AIAA-2008-0917, Reno, NV, January 7–10, 2008.

[29]Shenoy, R., Smith, M., and Park, M., "Unstructured Overset Mesh Adaptation with Turbulence Modeling for Unsteady Aerodynamic Interactions," *Journal of Aircraft*, Vol. to appear .

[30]Innovative Strategies for Rotary-Wing Coupled Aeroelastic Simulations, "NASA Langley Research Center," Award No. NNX07AP43A.

[31]Wissink, A. *et al.*, "Multi-Code Python-Based Infrastructure for Overset CFD with Adaptive Cartesian Grids," *46th AIAA Aerospace Sciences Meeting and Exhibit*, AIAA-2008-0927, Reno, NV, January 2008.

[32]Sitaraman, J., *et al.*, "Evaluation of a Multi-Solver Paradigm for CFD using Unstructured and Adaptive Cartesian Grids," *46th AIAA Aerospace Sciences Meeting and Exhibit*, AIAA-2008-0660, Reno, NV, January 2008.

[33]Shenoy, R., Holmes, M., Smith, M. J., and Komerath, N., "Scaling Evaluations on the Drag of a Hub System," *Journal of the American Helicopter Society*, Vol. to appear .